

# Space-confined charge transfer turns on multicolor emission in metal-organic frameworks via pressure treatment

Received: 1 January 2025

Accepted: 22 April 2025

Published online: 05 May 2025

Ting Zhang<sup>1,4</sup>, Yanfeng Yin<sup>2,4</sup>, Xinyi Yang<sup>1</sup>✉, Nuonan Li<sup>3</sup>, Weibin Wang<sup>1</sup>, Yunfeng Yang<sup>1</sup>, Wenming Tian<sup>2</sup>✉, Fuquan Bai<sup>3</sup>✉ & Bo Zou<sup>1</sup>✉

Single-component multi-emissive materials with stimuli-responsive properties offer unique advantages in the field of multicolor-tunable photoluminescence (PL). However, precisely modulating the emission of each component and achieving high-efficiency emission present a formidable challenge. Herein, we demonstrate that space-confined charge transfer (CT) turns on bright blue-green-white emission in initially faintly emissive metal-organic frameworks (MOFs) at ambient conditions through pressure treatments. Pressure treatments induce a transition from the initial long-range CT to a space-confined mode, significantly amplifying radiative transitions. Furthermore, the space-confined CT, which occurs between mutually perpendicular ligands, significantly influences the spin-orbit charge transfer intersystem crossing. Precise tuning of space-confined CT kinetics via multi-level pressure treatments allows us to modulate the fluorescence-to-phosphorescence ratio, achieving multicolor-tunable emission in the target MOFs. Our work advances the development of multicolor-tunable smart PL materials and unlocks the potential for their application in atmospheric environments.

The pursuit of multicolor-tunable photoluminescent (PL) materials is a promising frontier, offering substantial applications in multi-dimensional bioimaging, secure encryption, and sophisticated visual displays<sup>1–4</sup>. However, fabricating single-component PL materials capable of dynamically altering their emission is fraught with challenges. Complex design and tedious synthesis are usually required to suppress non-radiative channels and achieve dynamic emission responses. Stimulus-responsive materials possessing multiple emission properties provide a promising avenue for achieving multicolor-tunability<sup>5–9</sup>. The key to this endeavor lies in the precise control of chromophore conformation by external stimuli. Among various stimuli, pressure stands out for its ability to finely modulate molecular conformations, intermolecular interactions, electronic coupling, energy and charge

transfer (CT) pathways, thereby optimizing PL properties<sup>10–16</sup>. Recent studies have detailed that pressure treatment can significantly boost the emission of initially non-emitting or weakly emitting materials<sup>17–19</sup>. Yet, the quest to attain multicolor tunability in PL emissions at ambient conditions by pressure treatment is still in its infancy and represents a highly anticipated area of research.

Metal-organic frameworks (MOFs) constitute a compelling category of stimuli-responsive materials, characterized by their dynamic structural adaptability stemming from an array of tunable weak non-covalent interactions<sup>20–24</sup>. By appropriate design, the chromophores could be converted as organic ligands that coordinate with metal clusters or metal ions and anchored in framework structures<sup>25–29</sup>. Synergistic coordination between inorganic metal nodes and organic

<sup>1</sup>State Key Laboratory of High Pressure and Superhard Materials, Synergetic Extreme Condition High-Pressure Science Center, College of Physics, Jilin University, Changchun, China. <sup>2</sup>State Key Laboratory of Molecular Reaction Dynamics, Dalian Institute of Chemical Physics, Chinese Academy of Sciences, Dalian, China. <sup>3</sup>International Joint Research Laboratory of Nano-Micro Architecture Chemistry, Institute of Theoretical Chemistry and College of Chemistry, Jilin University, Changchun, China. <sup>4</sup>These authors contributed equally: Ting Zhang, Yanfeng Yin. ✉e-mail: [yangxinyi@jlu.edu.cn](mailto:yangxinyi@jlu.edu.cn); [tianwm@dicp.ac.cn](mailto:tianwm@dicp.ac.cn); [baiqf@jlu.edu.cn](mailto:baiqf@jlu.edu.cn); [zoubo@jlu.edu.cn](mailto:zoubo@jlu.edu.cn)

linkers confers the conformational diversity and electronic structure tunability to organic chromophores<sup>30–33</sup>. Stable and adaptive framework structure of MOFs provides a platform for precise control of spatial orientation, stacking pattern and molecular conformation of organic chromophores<sup>34</sup>. Abundant and tunable intermolecular interactions, energy and CT pathways in the framework offer the possibility of compelling emission behaviors<sup>35–38</sup>. MOFs hold great promise for modulating their crystal and electronic structures under external stimuli thereby affording opportunities for the development of multicolor-tunable PL materials<sup>39–42</sup>.

Here, we turn on bright blue-green-white emission in initially faintly emissive Cd(BDC)(DMF) (BDC: 1,4-benzenedicarboxylate, DMF: N,N-dimethylformamide) at ambient conditions by employing multi-level pressure treatments. The BDC linkers in Cd(BDC)(DMF) exhibit two distinct configurations, which provide excellent structure and performance tunability. Further, the  $n-\pi^*$  transition of carboxyl groups and the heavy-atom effects of Cd ions enable the potential for triplet exciton emission. Although Cd(BDC)(DMF) possesses the potential for multicolor tunable emission, ligand rotation results in very weak luminescence<sup>43–45</sup>. Pressure treatments induce a more compact spatial arrangement between ligands in the framework, which enhances hydrogen bonding and spatially confines the initial long-range CT. Enhanced hydrogen bonding restricts the rotation of the ligands and space-confined CT enhances the intensity of the radiative transition oscillator. Notably, engineered CT features a mutually perpendicular natural transition orbital configuration, which boosts the spin-orbit CT intersystem crossing process. Based on engineered CT, pressure treatments modulate the fluorescence-to-phosphorescence ratio and turn on multicolor emission. The turn-on of efficient multicolor emission in pressure-responsive smart materials is exceedingly rare after releasing the pressure completely. Our work provides innovative perspectives for designing high-efficiency, multicolor-tunable, stimulus-responsive smart PL materials.

## Results and discussion

### Crystal structure and PL stimuli-responsive behaviors of Cd(BDC)(DMF)

Cd(BDC)(DMF) possesses a triclinic  $P\bar{1}$  crystal structure and one-dimensional rhombic pore structures oriented along the  $a$ -axis<sup>46</sup>. Within this structure, linear aromatic dicarboxylic acid BDC ligands bridge cadmium ions using a mixed coordination mode of  $\kappa^1$ - and  $\kappa^2$ - to yield infinite chains. Each cadmium ion is 7-coordinated and bonded to two  $\kappa^1$ -carboxylates, two  $\kappa^2$ -carboxylates and a DMF ligand (Fig. 1a). As a representative aromatic ligand, BDC features carboxyl groups capable of  $n-\pi^*$  transitions and possesses fluorescence and phosphorescence bi-emissive properties in the rigid MOF (Supplementary Fig. 1). The BDC units in the rhombic network present “planar” and “distorted” conformations along the (010) and (01-1) crystalline planes, respectively. Distorted BDC displays a 33.1-degree dihedral angle between carboxyl group and benzene ring. The multi-configurational organic linker endows Cd(BDC)(DMF) with easily adjustable electronic properties. However, the PL performance of Cd(BDC)(DMF) is hampered by the non-radiative energy loss, owing to the rotation of BDC. Cd(BDC)(DMF) exhibits barely visible emission under ambient conditions (Supplementary Fig. 2).

Cd(BDC)(DMF) possesses an excellent stimulus-responsive potential owing to the flexible rhombic framework, abundant hydrogen bonds and coordination bonds. Given the tunable structure, the emissive properties of Cd(BDC)(DMF) can be modulated by adjusting the molecular conformation and intermolecular interaction in response to external stimuli. To validate our hypotheses, we perform in situ high-pressure PL experiments of Cd(BDC)(DMF). The PL intensity gradually increases when pressurized to 7.2 GPa. While above 7.2 GPa, the PL strength gradually declines and nearly quenches at 18.3 GPa (Supplementary Fig. 2 and Fig. 1b). A bright blue light

emission is captured to ambient conditions after completely releasing the pressure from 18.3 GPa (Fig. 1c). We intercept bright green and white light emission after the pressure is completely released from 26.1 and 30.0 GPa, respectively (Fig. 1d, e and Supplementary Fig. 3). Pressure treatment strategies turn on bright blue-green-white emission with chromaticity coordinates of (0.21, 0.27), (0.27, 0.34), and (0.30, 0.35) in initially faint Cd(BDC)(DMF) at ambient conditions (Fig. 1f). To reveal the path of intercepted bright multicolor emission, we further perform time-resolved PL spectroscopy and time-resolved PL decays measurements on the engineered Cd(BDC)(DMF) after pressure treatment. Engineered Cd(BDC)(DMF) exhibits fluorescence emission at 450 nm with lifetime of 4.0 ns and phosphorescence emissions at 520 nm with lifetime of 89.0 ms after pressure treatment of 18.0 GPa (Fig. 1g, h). Similarly, engineered Cd(BDC)(DMF) exhibits fluorescence emission at 450 nm with lifetime of 3.5 ns and phosphorescence emissions at 520 nm with lifetime of 84.2 ms after pressure treatment of 24.0 GPa (Supplementary Fig. 4). For higher pressure treatments, we are unable to get enough samples for the delayed emission and lifetime measurements, but we collect the PL spectra after the different pressure treatments to track the evolutionary behavior (Supplementary Fig. 5). The results show that the fluorescence proportion reduces while that of phosphorescence improves for the engineered Cd(BDC)(DMF) after higher pressure treatment. This is responsible for the change of emission color from blue to green and white. The turn-on of multicolor emission in pressure-treated Cd(BDC)(DMF) at ambient conditions provides a simple and robust strategy for the design and preparation of smart materials with efficient multicolor emission.

### Structural evolution of Cd(BDC)(DMF) under pressure

The intriguing emissive response behavior of Cd(BDC)(DMF) is intricately linked to the structural evolution under pressure. Characterized by a distinctive wine-rack architecture, Cd(BDC)(DMF) typically experiences negative compression with a reduction in the acute angles of rhombic framework under pressure<sup>47,48</sup>. To unravel the mechanisms behind the turn-on of bright multicolor emission after pressure treatment, we conduct in situ high-pressure angle dispersive X-Ray diffraction (ADXRD) experiments for Cd(BDC)(DMF) up to 30.0 GPa (Fig. 2a). Meanwhile, the Pawley refinements of ADXRD patterns as the pressure increases to 12.9 GPa and complete releases from 18.2 GPa are carried out (Supplementary Figs. 6–9). As expected, the Bragg diffraction peaks of the (001) crystalline plane undergo a shift from merged position about 4.10 degrees to 3.94 degrees at 0.1 GPa. This observation substantiates the negative compressive behavior of the wine-rack structure under pressure. Concurrently, there is a phase transition in Cd(BDC)(DMF) from  $P\bar{1}$  to  $P1$ , alongside significant compression of the  $a$ -axis within the layered structure (Supplementary Fig. 6). Upon reaching 9.4 GPa, the (001) crystal plane is almost immobile, while the others are continuously compacted. Upon further compression to 18.2 GPa, the (001) plane remains almost immobile. Above 18.2 GPa, the (001) crystal plane moves to a smaller angle, signifying further negative compression of the rhombic framework. At 30.0 GPa, Cd(BDC)(DMF) undergoes complete amorphization. In essence, the rhombic framework endures two significant compressions and the reduction in the interlayer distances under pressure. The varying extents of negative compression and inter-layer compression are retained to ambient conditions after complete release of pressure (Fig. 2b). The consequent pore constriction and layer closeness bring the ligands at rhombic edge getting into closer proximity, thereby triggering substantial changes in the intermolecular interactions in engineered Cd(BDC)(DMF).

To gain a direct insight into the evolution of intermolecular interactions under pressure, we conduct in situ high-pressure infrared (IR) spectra up to 30.3 GPa (Fig. 2c, d and Supplementary Fig. 10). Typically, the proximity of atoms induced by pressure leads to a

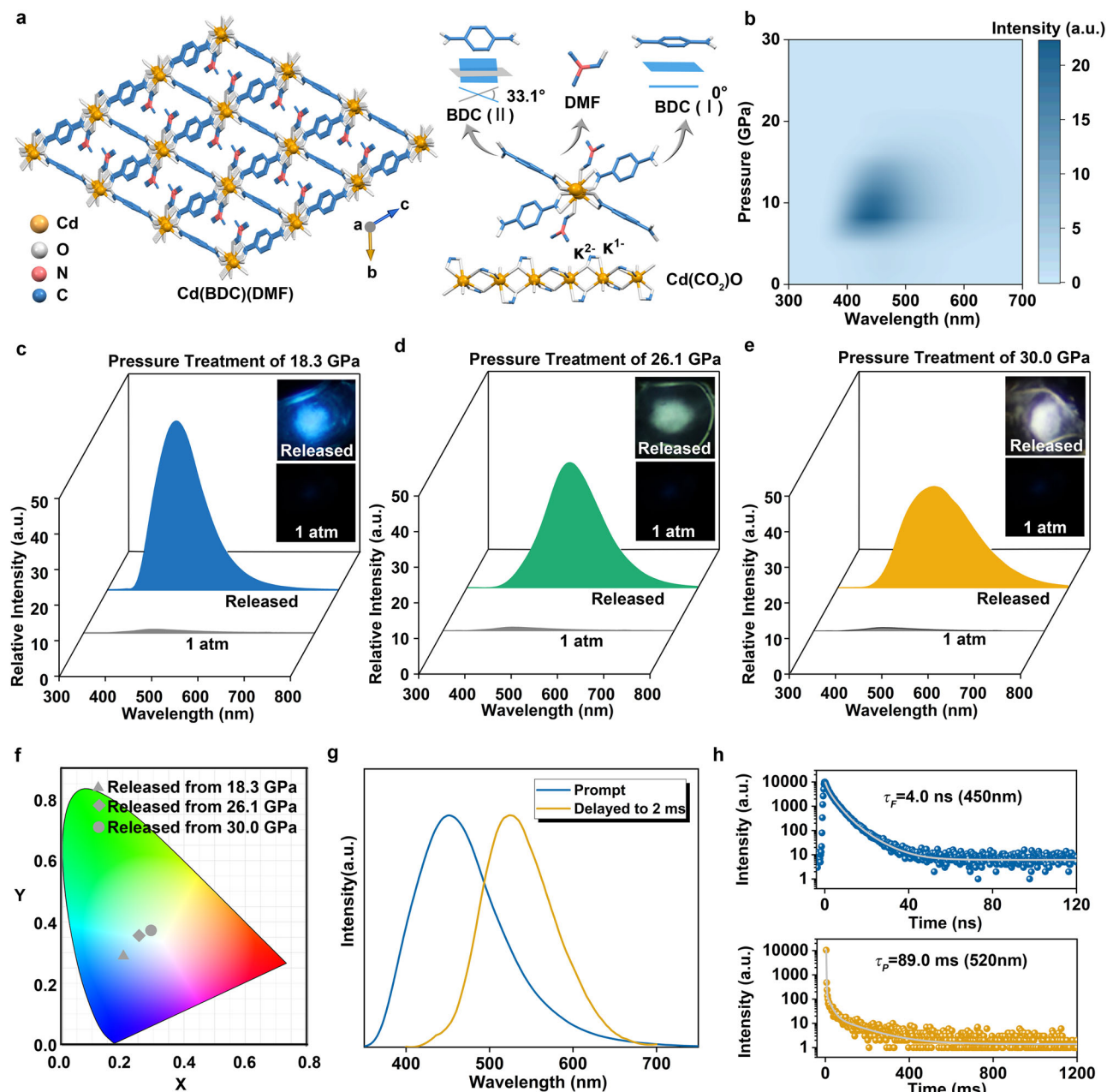


**Fig. 1 | The crystal structure and PL properties of Cd(BDC)(DMF).** **a** The crystal structure of Cd(BDC)(DMF) (H atoms are omitted for clarity) at ambient conditions. **b** 2D mapping of pressure-dependent PL intensity and wavelength of Cd(BDC)(DMF) (a.u. arbitrary units). PL spectra and corresponding PL photographs of Cd(BDC)(DMF) at 1 atm and after releasing pressure from **c** 18.3, **d** 26.1, and **e** 30.0 GPa. **f** Chromaticity coordinates of the PL for engineered Cd(BDC)(DMF) after releasing pressure from 18.3, 26.1, and 30.0 GPa. **g** Normalized prompt and delayed to 2 ms PL spectra, **h** PL decay curves of Cd(BDC)(DMF) after 18.0 GPa pressure treatment by the Walker-Type Large-Volume Press.

continuous shift of the vibrational peaks in IR absorption towards higher wavenumbers. However, in the case of Cd(BDC)(DMF), the IR spectra show that the out-of-plane bending vibration of aromatic C–H,  $\delta_{\text{op}}(\text{C–H})$ , at  $878\text{ cm}^{-1}$  exhibits a redshift under pressure<sup>49</sup>. Additionally, the out-of-plane bending vibration of carboxyl group at  $820\text{ cm}^{-1}$ ,  $\delta_{\text{op}}(\text{O–C–O})$ <sup>50</sup>, splits into new vibrational peak positions towards lower wavelengths, specifically at  $811\text{ cm}^{-1}$ . Upon releasing pressure from 18.4, 25.2, and 30.3 GPa, the new  $\delta_{\text{op}}(\text{O–C–O})$  peaks are retained, while the engineered  $\delta_{\text{op}}(\text{C–H})$  peak exhibits a redshift of 12.0, 12.2, and  $10.1\text{ cm}^{-1}$ , respectively, compared to that before pressure treatment. This observation aligns with the preserved deformation of the rhombic framework as shown in ADXRD patterns after pressure treatment. In combination with crystal structure analysis, the restriction of these IR

vibrations is attributed to enhanced hydrogen bonding between the carboxyl C–O and the aromatic C–H of the BDCs on the acute sides of the rhombic framework. In addition, in situ high-pressure Raman scattering spectra reveal that some of Raman peaks of Cd(BDC)(DMF) undergo broadening and disappearance under pressure, indicating pressure-induced lattice distortion (Supplementary Fig. 11). The distortion can not be fully recovered after pressure release, which is consistent with the analysis of ADXRD patterns. Furthermore, utilizing the crystal structure obtained from the refined ADXRD pattern after complete decompression from 18.2 GPa, we have generated the corresponding Hirshfeld surfaces of engineered BDC units (Fig. 2e). The enlarged red regions on these surfaces indicate stronger C–H $\cdots$ O–C hydrogen bonding between BDC units. Up to 7.2 GPa, enhanced



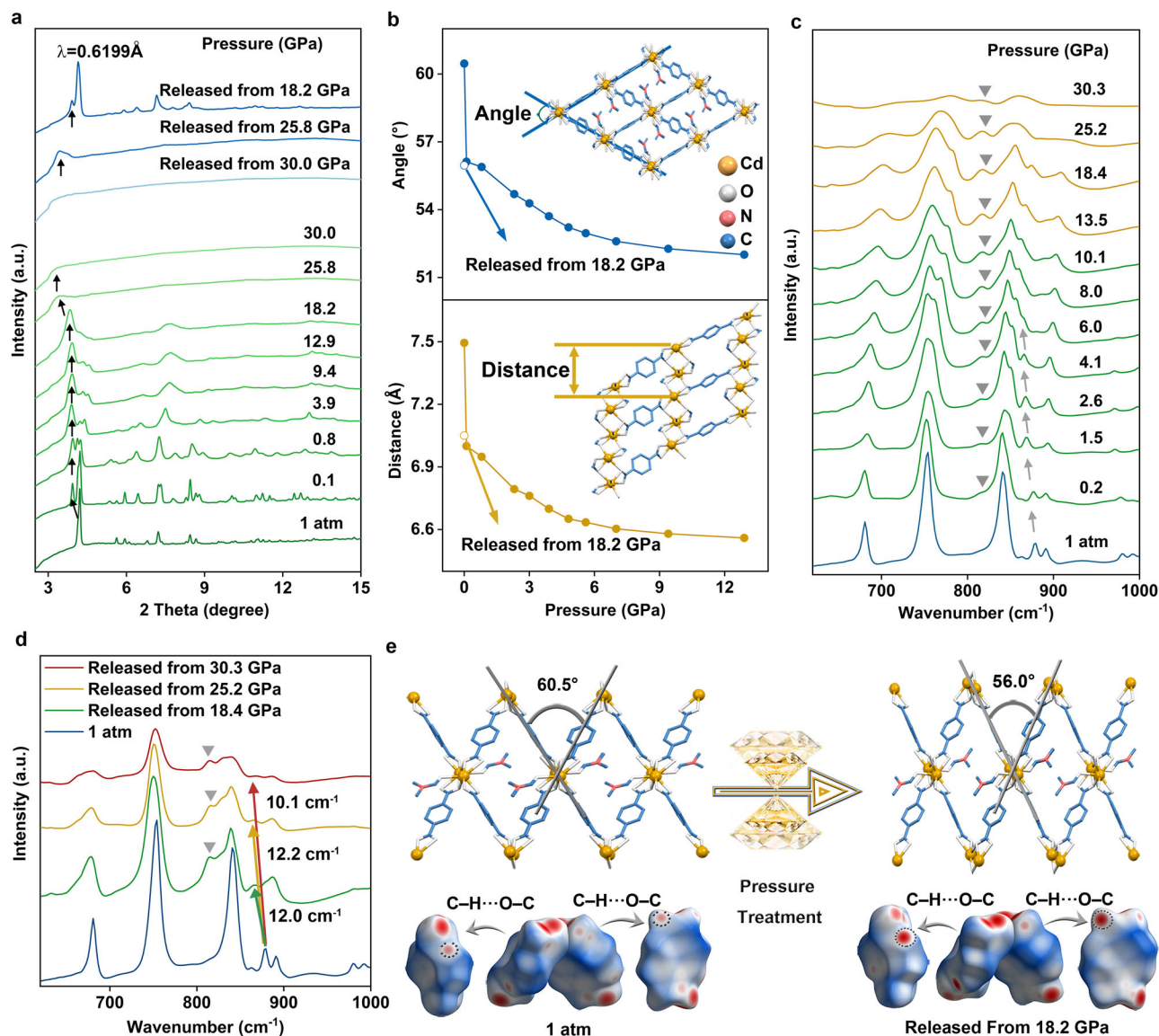


**Fig. 2 | Crystal structure evolution of Cd(BDC)(DMF) with pressure.** **a** Selected ADXRD patterns of Cd(BDC)(DMF) at different pressures. **b** Evolution of the acute angle within rhombus and the distance between rhombic layers in Cd(BDC)(DMF) structure with pressure. The amplified IR spectra from 620 to 1000  $\text{cm}^{-1}$  of Cd(BDC)(DMF) (**c**) during compression, **d** at 1 atm and after releasing pressure from

18.4, 25.2, and 30.3 GPa. **e** Schematic diagram of the structure and the Hirshfeld surfaces for BDCs with a  $d_{\text{norm}}$  distance of Cd(BDC)(DMF) before and after pressure treatment of 18.2 GPa. The black arrows, gray triangles, and gray arrows indicate the changes in the (001) crystal plane,  $\delta_{\text{op}}(\text{O}-\text{C}-\text{O})$ , and  $\delta_{\text{op}}(\text{C}-\text{H})$  with pressure, respectively.

hydrogen bonding restricts the vibration of framework and the rotation of ligand, resulting in the reduction of non-radiative transition and the enhancement of PL. However, severe structural distortions lead to quenching of emission under higher pressures. After the pressure is fully released, the preservation of the enhanced hydrogen bonding is responsible for the bright emission.

### Theoretical calculation of Cd(BDC)(DMF)

The rhombic framework structure, characterized by narrower acute angles and enhanced hydrogen bonding, facilitates enhanced electronic coupling between the ligands along the acute edges of the rhombus. To elucidate the modifications in the electronic structure, we perform frontier orbitals calculations on periodic structure of Cd(BDC)(DMF) after pressure treatment of 18.2 GPa. The density functional theory calculations reveal pronounced charge delocalization in the engineered Cd(BDC)(DMF) (Supplementary Fig. 12). The valence band maximum mainly populates on the planar BDC, while the conduction band minimum is delocalized on twisted BDC.

Consequently, the intra-ligand CT from “planar” to “twisted” BDC units is observed in engineered Cd(BDC)(DMF). Further, we carry out a thorough analysis of the singlet and triplet excited state energies for Cd(BDC)(DMF) before and after pressure treatment of 18.2 GPa to assess the influence of CT on phosphorescence and fluorescence emissions. Time-dependent density-functional theory (TD-DFT) calculations indicate that pressure treatment spatially confines the initially long-range CT (Fig. 3a). Meanwhile, the oscillator strength of  $S_1$  and  $S_2$  in the engineered Cd(BDC)(DMF) are significantly increased to 0.7096 and 0.0125 from the initial 0.0221 and 0.0065, respectively (Fig. 3b). The spatial confinement of extensive CT enhances the transition localization and intensity, which accounts for the bright emission of Cd(BDC)(DMF) after pressure treatment. Most notably, the HOMO and LUMO orbitals are arranged in planar and twisted BDC cells, respectively, exhibiting mutually perpendicular spatial orientations. This charge recombination leads to a significant variation in orbital angular momentum. According to the spin-orbit charge transfer intersystem crossing (SOCT-ISC) mechanism, this combination

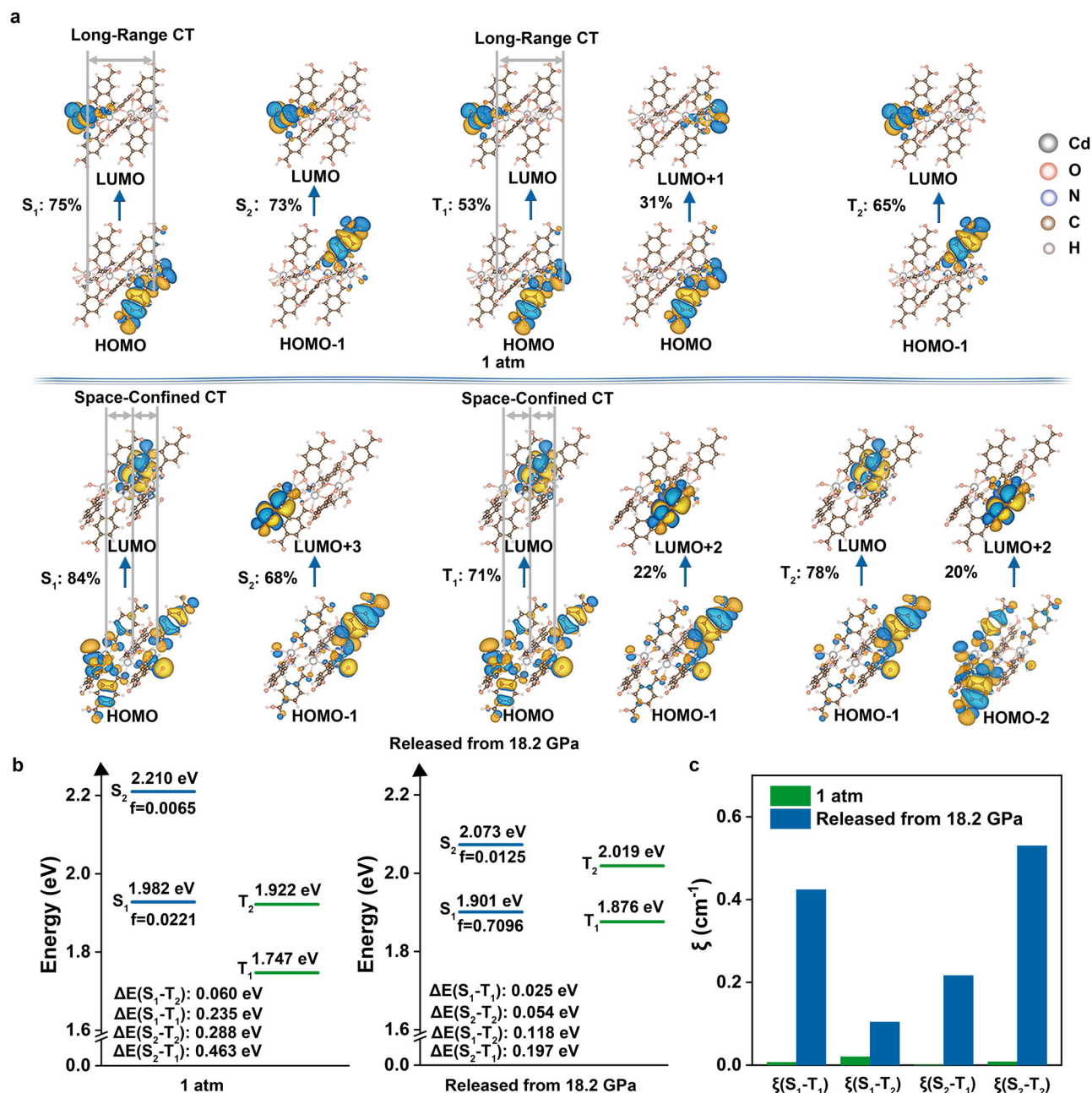


**Fig. 3 | Time-dependent DFT calculation results of Cd(BDC)(DMF).** **a** The frontier natural transition orbitals and **b** energy levels of  $S_1$ ,  $T_1$ ,  $S_2$ ,  $T_2$  for Cd(BDC)(DMF) before and after pressure treatment of 18.2 GPa. **c** The spin-orbit coupling degree of

$\xi(S_1-T_1)$ ,  $\xi(S_1-T_2)$ ,  $\xi(S_2-T_1)$ , and  $\xi(S_2-T_2)$  for Cd(BDC)(DMF) before and after pressure treatment of 18.2 GPa.  $S_1$ : first singlet,  $T_1$ : the first triplet,  $S_2$ : second singlet,  $T_2$ : second triplet states.

requires a large spin-orbit coupling (SOC)<sup>51–54</sup>. As expected, after pressure treatment of 18.2 GPa, the SOC constants  $\xi(S_1-T_1)$ ,  $\xi(S_1-T_2)$ ,  $\xi(S_2-T_1)$ , and  $\xi(S_2-T_2)$  increase to 0.4241, 0.1042, 0.2167, and 0.5301 cm<sup>-1</sup> from the initial 0.0071, 0.0205, 0.0009, and 0.0083 cm<sup>-1</sup>, respectively (Fig. 3c). Furthermore, pressure treatment effectively modulates the energy levels of this MOF, reducing the energy differences  $\Delta E(S_1-T_1)$ ,  $\Delta E(S_2-T_1)$ , and  $\Delta E(S_2-T_2)$  from the initial 0.235, 0.463, and 0.288 eV to 0.025, 0.197, and 0.054 eV. The combined effects of enhanced oscillator strength in the singlet state, robust SOC, and reduced energy gap between singlet and triplet states collectively contribute to the marked enhancement of phosphorescence emission.

### Electronic structure of Cd(BDC)(DMF) in response to pressure

The engineered Cd(BDC)(DMF) exhibits partial or complete amorphization after pressure treatment exceeding 18.2 GPa, despite

exhibiting a more pronounced degree of negative compression structure. We could not obtain the corresponding crystal structures for theoretical calculations to reveal the CT process. Nonetheless, the absorption spectra of Cd(BDC)(DMF) after different pressure treatments display enhanced band tails, which are consistent with the formation of localized and intense CT<sup>55,56</sup>. As well, the enhancement of the absorption band tails during pressurization suggests the localization of the CT (Supplementary Fig. 13). Notably, the engineered Cd(BDC)(DMF) presents a more pronounced absorption band tail as the pressure treatment values increase from 18.1 to 26.2 and 30.2 GPa (Fig. 4a). To further investigate the CT dynamics, femtosecond transient absorption (fs-TA) measurements are conducted on engineered Cd(BDC)(DMF) after pressure treatments (Fig. 4b). The fs-TA spectra of engineered Cd(BDC)(DMF) exhibit a broad photoinduced absorption signal peaked at 550 nm, which can be assigned as the excitonic-

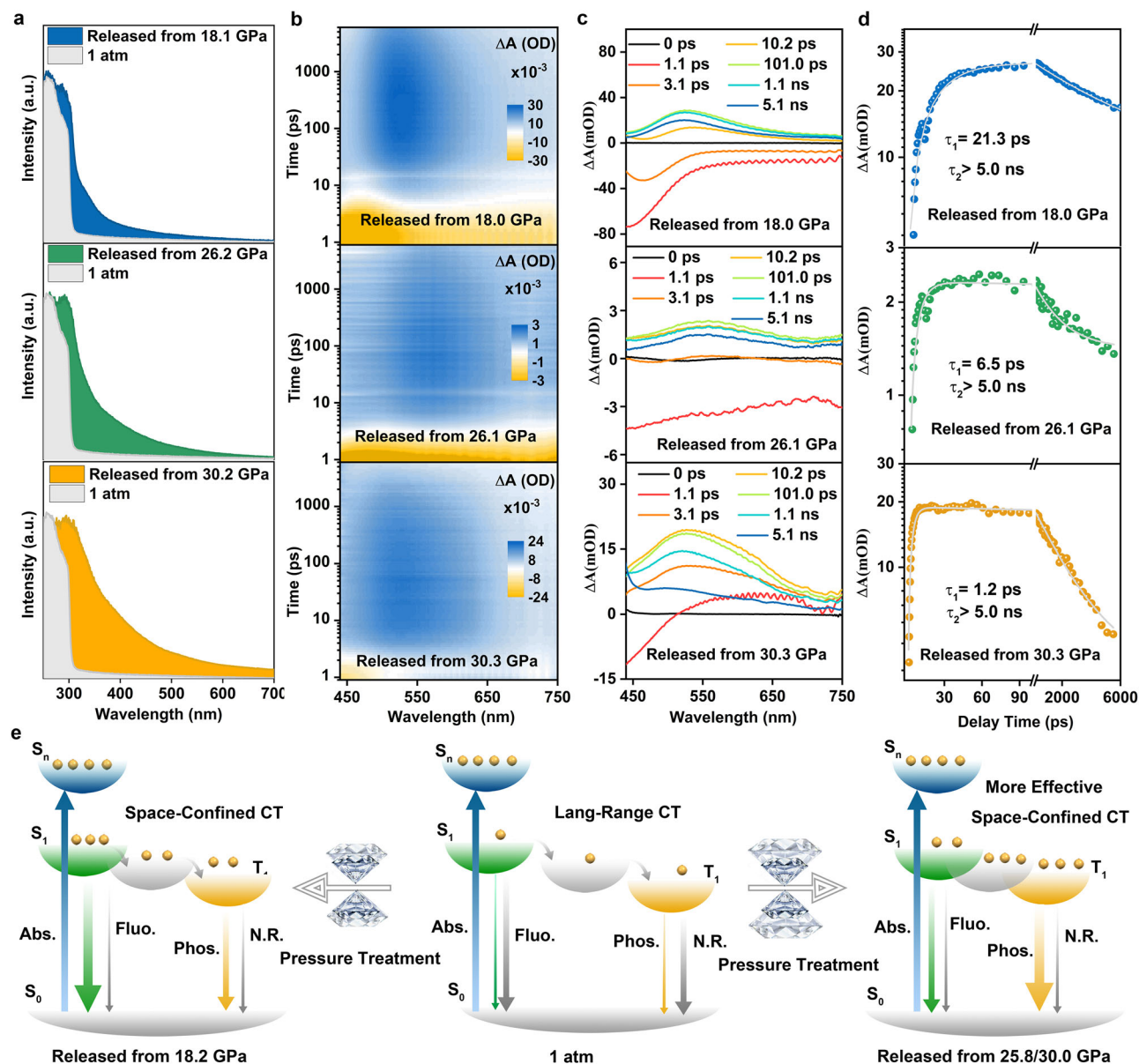


**Fig. 4 | Electronic structure evolution and PL modulation mechanism of Cd(BDC)(DMF).** **a** UV/Vis absorption spectra of Cd(BDC)(DMF) at 1 atm and after pressure is released from 18.1, 26.2, 30.2 GPa. **b** Pseudocolor TA plot of engineered Cd(BDC)(DMF). **c** Selected TA spectra at different delay times. **d** TA kinetics of

engineered Cd(BDC)(DMF) probed at 550 nm and the solid lines are the fits of the kinetics. **e** Schematic diagram of space-confined CT turn-on multicolor-tunable emission. Abs. absorption, Fluo. fluorescence, Phos. phosphorescence, N.R. non-radiation.

state absorption (ESA) (Fig. 4b). The time evolution of fs-TA spectra of engineered Cd(BDC)(DMF) implies a transition of carriers from excitons to the ESA state (Fig. 4c). The CT process can be seen in their TA kinetics probed at 550 nm (Fig. 4d). Within the initial ~90 ps, the TA kinetics exhibit a fast rising component, further substantiating the formation of the charge-transfer state. Global fitting of these TA kinetics reveals a fast charge-transfer component along with a decay component. Notably, the charge-transfer time of engineered Cd(BDC)(DMF) markedly shortens with increased pressure treatment values from 18.0 GPa to 26.1 GPa and 30.3 GPa. This indicates that Cd(BDC)(DMF) after elevated pressure treatment possesses more efficient CT, thereby more intense SOCT-ISC. The enhancement of SOC causes an increase of the phosphorescence emission proportion, which accounts for the conversion from blue to green and white light emission when the pressure treatment values are increased from 18.3 to 26.1 and 30.0 GPa (Fig. 4e).

To illustrate the stability of engineered Cd(BDC)(DMF) as a luminescent material, a white phosphor-converted light-emitting diode (pc-LED) device is fabricated by encapsulating Cd(BDC)(DMF) after pressure treatment of 30.0 GPa above a 365 nm UV-emissive chip (Fig. 5a). The fabricated pc-LED shows bright white light emission with chromaticity coordinates of (0.29, 0.34) (Fig. 5b, c). The emission spectrum and chromaticity coordinate of the white pc-LED match those of the Cd(BDC)(DMF) after pressure treatment of 30.0 GPa. We further test the stability of the white pc-LED. Upon increasing current from 10 to 90 mA, the emission intensity of white pc-LED steadily increases, demonstrating excellent color stability (Fig. 5d). Moreover, the white pc-LEDs exhibited high fatigue stability with slight changes in emission intensity for 72 h at ambient conditions (Fig. 5e).

In summary, we have turned on brilliant blue-green-white emission in initially faintly emissive Cd(BDC)(DMF) by applying



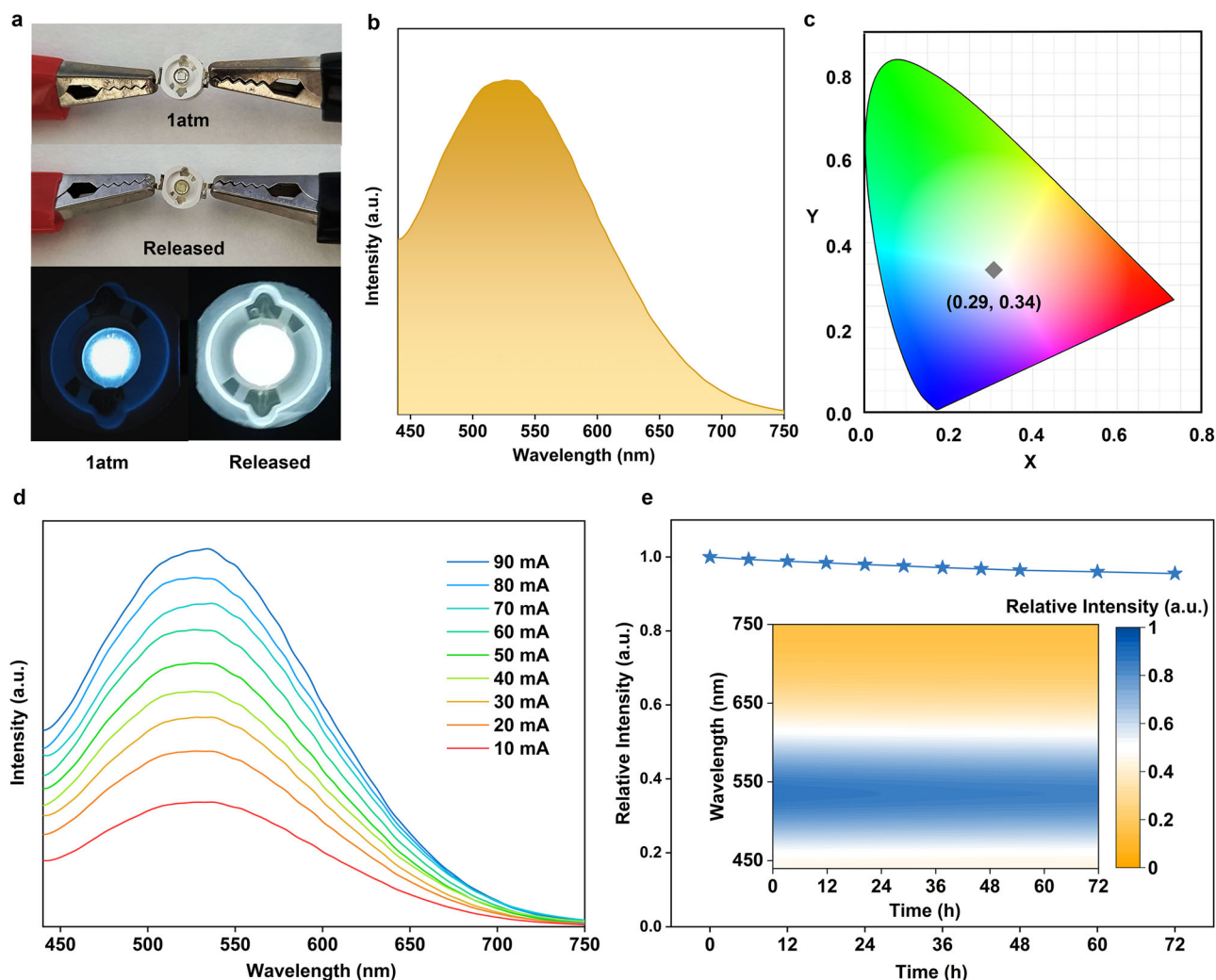


**Fig. 5 | Stability of engineered Cd(BDC)(DMF) as a luminescent material.**

**a** Photographs of the operating white pc-LED device. **b** PL spectrum of the fabricated white pc-LED. **c** CIE chromaticity coordinates of the fabricated white pc-LED.

**d** PL spectra of the white pc-LED at a low voltage (3.1 V) and various operating currents. **e** Integrated PL intensity of the white pc-LED as a function of aging time. The inset shows the visual time-quenching behavior.

multiple pressure treatments. Comprehensive structural analysis and theoretical calculations reveal that the rhombic frameworks of Cd(BDC)(DMF) undergo negative compressions after different pressure treatments. Negative compressions lead to enhancement of hydrogen bonding between ligands on the acute edges of frameworks, which plays a key role in restricting the vibration and rotation of the frameworks. Additionally, pressure treatments modulate the CT by enhancing the electronic coupling between the ligands. The initial long-range CT is transformed into space-confined CT after pressure treatment, thus increasing the localization and intensity of the transitions. Enhanced hydrogen bonding and space-confined CT are responsible for the bright emission of the initially faintly emissive Cd(BDC)(DMF) at ambient conditions. Higher pressure treatments have been observed to accelerate the process of CT and SOCT-ISC, thus promoting phosphorescence emission. By precisely controlling the proportion of fluorescence to phosphorescence, we achieve bright blue-green-white emission in initially faintly emissive Cd(BDC)(DMF) after pressure release from 18.3, 26.1, and 30.0 GPa. The tunable multicolor emission at ambient conditions provides valuable insights and a platform for designing and preparing smart materials with efficient multicolor emission.

## Methods

### Sample preparation

Cd(BDC)(DMF) is synthesized through a refined version of an existing synthetic protocol<sup>46</sup>. Cd(NO<sub>3</sub>)<sub>2</sub>·4H<sub>2</sub>O (0.308 g, 1.0 mmol) and H<sub>2</sub>BDC (0.166 g, 1.0 mmol) are dissolved in DMF (10 mL). After a solvothermal reaction at 125 °C for 12 h in a Teflon-Steel autoclave, obtained crystals are washed by DMF. All the reagents and solvents used in this synthesis are available commercially and used without further purification.

### Optical measurement

PL decay curves and time-resolved PL spectroscopy are measured by using Edinburgh FLS920. The pressure-treated Cd(BDC)(DMF) sample used for PL decay curves, and time-resolved PL spectroscopy measurement is obtained using a Walker type large volume press.

Fs-TA measurements are measured with a regenerative amplified Ti: sapphire laser system from Coherent (800 nm, 35 fs, 6 mJ/pulse, and 1 kHz repetition rate), nonlinear frequency mixing techniques and the Femto-TA100 spectrometer (Time-Tech spectra). The pressure-treated Cd(BDC)(DMF) sample used for fs-TA spectroscopy measurement is obtained by diamond anvil cell (DAC).

## The fabrication process of white pc-LED device

The Cd(BDC)(DMF) samples are blended with epoxy resin adhesive at a weight ratio of 10% and manually stirred using a stainless steel rod for 3 min until complete homogeneity. The mixture is subsequently applied onto the surface of the commercial UV chip until complete filling of the microcavity occurred. Finally, the solid-state lighting units are cured in the oven at a temperature of 35 °C. These chips, purchased from the Shenzhen Looking Long Technology Co., Ltd. (Shenzhen, China), possess a power of 1 W and an excitation wavelength of 365 nm. The performance of the prepared pc-LED devices is measured using an automatic temperature LED photo analyzer equipped with a precise temperature controller (ATA-500, EVERFINE, China). The pressure-treated Cd(BDC)(DMF) sample used for fabricating pc-LEDs is obtained by using a Paris-Edinburgh press and double toroidal sintered diamond anvils.

## In situ high-pressure measurements

All in situ high-pressure experiments are carried out with symmetric DAC apparatus furnished with a pair of 400  $\mu\text{m}$  culet diamonds at room temperature. A hole of the T301 stainless-steel compressible gasket with about 140  $\mu\text{m}$  diameter, which is pre-indented to a thickness of 40  $\mu\text{m}$ , is used to enclose the Cd(BDC)(DMF) sample. Pressure determination is achieved by the R1 fluorescence spectrum of the ruby.

In situ high-pressure PL and UV-visible absorption spectra of Cd(BDC)(DMF) are recorded by an optical fiber spectrometer (Ocean Optics, QE65000). PL photographs of Cd(BDC)(DMF) are obtained using a camera (Canon Eos 5D mark II) equipped on a microscope (Eclipse TI-U, Nikon). The excitation sources of a 355 nm line of a UV DPSS laser and a Deuterium-Halogen light are respectively used for PL and UV-visible absorption measurements. Silicon oil (Aldrich) is utilized as the pressure transmitting medium (PTM) in the high-pressure PL and UV-visible absorbance experiments.

In situ ADXRD experiments of Cd(BDC)(DMF) are performed with an incident monochromatic wavelength of 0.6199 Å at beamline 15U1, Shanghai Synchrotron Radiation Facility.  $\text{CeO}_2$  is utilized as the standard sample for the calibration. The pattern of intensity versus diffraction angle 2-theta is recorded and analysed by Dioptas program.

In situ high-pressure IR absorption measurement of Cd(BDC)(DMF) is carried out at room temperature using a Bruker Vertex 70 V FT-IR spectrometer (BRUKER OPTIK GMBH, Germany) equipped with a nitrogen-cooled mercury-cadmium-telluride detector. KBr is used as PTM in IR experiments.

In situ high-pressure Raman spectroscopy measurements are carried out using a Raman spectrometer (iHR 550, Symphony II, Horiba Jobin Yvon) with a 785 nm and 0.5 mW excitation laser.

## Hirshfeld Surface theory calculations

The structure of Cd(BDC)(DMF) is determined by synchrotron X-ray crystallographic analysis. The Crystal Explorer 17.5 program is used to visualize and analyze the intermolecular interactions in the crystal structures of Cd(BDC)(DMF) before and after pressure treatment<sup>57</sup>. It enables us to construct the 3-dimensional Hirshfeld surfaces of molecules in crystals.

## Density functional theory (DFT) calculations

DFT calculations of the frontier orbitals for Cd(BDC)(DMF) are conducted using the Materials Studio software with the Fukui functional and GGA/PLYP basis set.

## Time-dependent DFT calculations

The band structure of Cd(BDC)(DMF) system is calculated based on the first-principles and performed by Vienna ab initio simulation package<sup>58,59</sup>. Projector-augmented-wave employs to consider the electron-ion interactions, Perdew-Burke-Ernzerhof exchange correlation functional in the scheme of generalized gradient approximation

(GGA) with 400 eV as the cutoff energy of the plane-wave basis is implemented<sup>60</sup>. The molecular orbital and electron excited transition characteristics information are obtained from the time-dependent DFT calculation with  $\omega\text{B97XD}$  level<sup>61–65</sup>. Based on their geometric structures, their orbital energy variation and the orbital profiles of the systems under different pressures are calculated to study the effect of pressure. The influence of crystal environment can be seemed as perturbation term to the core MOFs skeleton. Traditional ONIOM(QM/MM) method faces many difficulties which are hard to reach the convergent limit<sup>66,67</sup>. As a result, the impact of environment is manifested in the polarity or the electric field effect which cause the calculation need to introduce an approximate method considering the circumambient electric field. Among all charges around the central fragment fit to the electrostatic potential. Charges from Electrostatic Potentials using a Grid based method (CHELPG) is the most common and famous charge for background charge analysis to describe the effect of surrounding groups in electronic structure properties<sup>68,69</sup>. As a first step of the fitting procedure, the electrostatic potential is calculated at a number of grid points spaced 3 pm apart and distributed regularly in a cube. The dimensions of the cube are chosen such that the structures are located at the center of the cube. All points falling inside the van-der-Waals radius of the modelling system are discarded from the fitting procedure.

## Reporting summary

Further information on research design is available in the Nature Portfolio Reporting Summary linked to this article.

## Data availability

The authors declare that the main data underlying all results in the manuscript and the Supplementary Information are provided in the Supplementary Source Data file. Source data are provided with this paper.

## Code availability

VASP code is available for download on the developer page: <https://www.vasp.at/>.

## References

- MacKenzie, L. E. & Pal, R. Circularly polarized lanthanide luminescence for advanced security inks. *Nat. Rev. Chem.* **5**, 109–124 (2021).
- Yakunin, S. et al. Radiative lifetime-encoded unicolour security tags using perovskite nanocrystals. *Nat. Commun.* **12**, 981 (2021).
- Nie, F. & Yan, D. Zero-dimensional halide hybrid bulk glass exhibiting reversible photochromic ultralong phosphorescence. *Nat. Commun.* **15**, 5519 (2024).
- Ma, Y. et al. Dynamic metal-ligand coordination for multicolour and water-jet rewritable paper. *Nat. Commun.* **9**, 3 (2018).
- Shi, Y. et al. Multiple yet switchable hydrogen-bonded organic frameworks with white-light emission. *Nat. Commun.* **13**, 1882 (2022).
- Xing, C., Zhou, B., Yan, D. & Fang, W. H. Dynamic photoresponsive ultralong phosphorescence from one-dimensional halide micro-rods toward multilevel information storage. *CCS Chem.* **5**, 2866–2876 (2023).
- Tang, X. et al. Highly efficient luminescence from space-confined charge-transfer emitters. *Nat. Mater.* **19**, 1332–1338 (2020).
- Yagai, S. et al. Design amphiphilic dipolar  $\pi$ -systems for stimuli-responsive luminescent materials using metastable states. *Nat. Commun.* **5**, 4013 (2014).
- Hanaoka, K. et al. A general fluorescence off/on strategy for fluorogenic probes: steric repulsion-induced twisted intramolecular charge transfer (sr-TICT). *Sci. Adv.* **10**, eadi8847 (2024).



10. Dewaele, A. et al. Synthesis and stability of xenon oxides  $\text{Xe}_2\text{O}_5$  and  $\text{Xe}_3\text{O}_2$  under pressure. *Nat. Chem.* **8**, 784–790 (2016).
11. Guo, S. et al. Reconfiguring band-edge states and charge distribution of organic semiconductor-incorporated 2D perovskites via pressure gating. *Sci. Adv.* **8**, eadd1984 (2022).
12. Guo, S. W. et al. Exciton engineering of 2D ruddlesden-popper perovskites by synergistically tuning the intra and interlayer structures. *Nat. Commun.* **15**, 3001 (2024).
13. Fu, T. et al. Manipulating peierls distortion in van der Waals  $\text{NbOX}_2$  maximizes second-harmonic generation. *J. Am. Chem. Soc.* **145**, 16828–16834 (2023).
14. Mao, Y. et al. Pressure-modulated anomalous organic-inorganic interactions enhance structural distortion and second-harmonic generation in  $\text{MHPbBr}_3$  perovskite. *J. Am. Chem. Soc.* **145**, 23842–23848 (2023).
15. Wang, W. et al. Brightening blue photoluminescence in non-emission phthalic anhydride by pressure-driven molecular reassembly. *Laser Photonics Rev.* **19**, 2401173 (2025).
16. Yang, Y. et al. Regulating planarized intramolecular charge transfer for efficient singlephase white-light emission in undoped metal-organic framework nanocrystals. *Nano. Lett.* **24**, 9898–9905 (2024).
17. Ma, Z. et al. Pressure-induced emission of cesium lead halide perovskite nanocrystals. *Nat. Commun.* **9**, 4506 (2018).
18. Zhang, T. et al. Brightening blue photoluminescence in non-emission MOF-2 by pressure treatment engineering. *Adv. Mater.* **35**, 2211729 (2023).
19. Xiao, Z. H. et al. Harvesting multicolor photoluminescence in non-aromatic interpenetrated metal-organic framework nanocrystals via pressure-modulated carbonyls aggregation. *Adv. Mater.* **36**, 2403281 (2024).
20. Wang, Z., Mo, J. T., Pan, J. J. & Pan, M. White light and color-tuning long persistent luminescence from metal halide based metal-organic frameworks. *Adv. Funct. Mater.* **33**, 2300021 (2023).
21. Dong, J., Wee, V. & Zhao, D. Stimuli-responsive metal-organic frameworks enabled by intrinsic molecular motion. *Nat. Mater.* **21**, 1334–1340 (2022).
22. Andreeva, A. B. et al. Soft mode Metal-linker dynamics in carboxylate MOFs evidenced by variable-temperature infrared spectroscopy. *J. Am. Chem. Soc.* **142**, 19291–19299 (2020).
23. Su, Y.-S. et al. Dipolar order in an amphidynamic crystalline metal-organic framework through reorienting linkers. *Nat. Chem.* **13**, 278–283 (2021).
24. Bonneau, M. et al. Tunable acetylene sorption by flexible catenated metal-organic frameworks. *Nat. Chem.* **14**, 816–822 (2022).
25. Wang, Z., Liu, J. J., Li, M. Y. & Chen, G. White light and long persistent luminescence from metal cluster-based metal-organic frameworks. *Chem. Eng. J.* **462**, 142154 (2023).
26. Wang, Z. et al. A metal-organic supramolecular box as a universal reservoir of UV, WL, and NIR light for long persistent luminescence. *Angew. Chem. Int. Ed.* **58**, 3481–3485 (2019).
27. Wang, Z. et al. Ultralong near infrared room temperature phosphorescence in  $\text{Cu(I)}$  metal-organic framework based-on D- $\pi$ -A- $\pi$ -D linkers. *Adv. Funct. Mater.* **33**, 2212985 (2023).
28. Yu, Q. et al. Ligand meta-anchoring strategy in metal-organic frameworks for remarkable promotion of quantum yields. *Angew. Chem. Int. Ed.* **63**, e202401261 (2024).
29. Chen, Z. et al. Reticular synthesis of one-dimensional covalent organic frameworks with 4-c sql topology for enhanced fluorescence emission. *Angew. Chem. Int. Ed.* **62**, e202213268 (2023).
30. Wei, Z. et al. Rigidifying fluorescent linkers by metal-organic framework formation for fluorescence blue shift and quantum yield enhancement. *J. Am. Chem. Soc.* **136**, 8269–8276 (2014).
31. Yao, Z. Q. et al. Dynamic full-color tuning of organic chromophore in a multi-stimuli-responsive 2D flexible MOF. *Angew. Chem. Int. Ed.* **61**, e202202073 (2022).
32. Huang, R. W. et al. Hypersensitive dual-function luminescence switching of a silver-chalcogenolate cluster-based metal-organic framework. *Nat. Chem.* **9**, 689–697 (2017).
33. Sun, K. et al. Dynamic structural twist in metal-organic frameworks enhances solar overall water splitting. *Nat. Chem.* **16**, 1638–1646 (2024).
34. Ye, Q. et al. Photoinduced dynamic ligation in metal-organic frameworks. *J. Am. Chem. Soc.* **146**, 101–105 (2024).
35. Wang, Z. et al. White-light emission from dual-way photon energy conversion in a dye-encapsulated metal-organic framework. *Angew. Chem. Int. Ed.* **58**, 9752–9757 (2019).
36. Geng, L. et al. Donor-acceptor metal-organic frameworks featuring tunable triplet states for multistimulus responsive room-temperature charge transfer phosphorescence. *CCS Chem.* **7**, 416–428 (2025).
37. Zhang, Y. et al. Near-unity energy transfer from uranyl to europium in a heterobimetallic organic framework with record-breaking quantum yield. *J. Am. Chem. Soc.* **145**, 13161–13168 (2023).
38. Zou, H., Hai, Y., Ye, H. & You, L. Dynamic covalent switches and communicating networks for tunable multicolor luminescent systems and vapor-responsive materials. *J. Am. Chem. Soc.* **141**, 16344–16353 (2019).
39. Liu, S., Lin, Y. & Yan, D. Dynamic multi-color long-afterglow and cold-warm white light through phosphorescence resonance energy transfer in host-guest metal-organic frameworks. *Sci. China Chem.* **66**, 3532–3538 (2023).
40. Ma, Y. J., Fang, X., Xiao, G. & Yan, D. Dynamic manipulating space-resolved persistent luminescence in core-shell MOFs heterostructures via reversible photochromism. *Angew. Chem. Int. Ed.* **61**, e202114100 (2022).
41. Zhou, B. & Yan, D. Long persistent luminescence from metal-organic compounds: state of the Art. *Adv. Funct. Mater.* **33**, 2300735 (2023).
42. Wang, Z. et al. Multi-mode color-tunable long persistent luminescence in single-component coordination polymers. *Angew. Chem. Int. Ed.* **60**, 2526–2533 (2021).
43. Yang, X. & Yan, D. Strongly enhanced long-lived persistent room temperature phosphorescence based on the formation of metal-organic hybrids. *Adv. Opt. Mater.* **4**, 897–905 (2016).
44. Yang, X. & Yan, D. Long-afterglow metal-organic frameworks: reversible guest-induced phosphorescence tunability. *Chem. Sci.* **7**, 4519–4526 (2016).
45. Ryder, M. R. et al. Detecting molecular rotational dynamics complementing the low-frequency terahertz vibrations in a zirconium-based metal-organic framework. *Phys. Rev. Lett.* **118**, 255502 (2017).
46. Burrows, A. D. et al. Syntheses, structures and properties of cadmium benzenedicarboxylate metal-organic frameworks. *Dalton Trans.* **18**, 2465–2474 (2008).
47. Wang, C. Z. et al. Pore size modulation in flexible metal-organic framework enabling high performance gas sensing. *Angew. Chem. Int. Ed.* **62**, e202302996 (2023).
48. Zeng, Q., Wang, K. & Zou, B. Large negative linear compressibility in  $\text{InH(BDC)}_2$  from framework hinging. *J. Am. Chem. Soc.* **139**, 15648–15651 (2017).
49. Zhou, X. et al. Molecular scalpel to chemically cleave metal-organic frameworks for induced phase transition. *J. Am. Chem. Soc.* **143**, 6681–6690 (2021).
50. Chang, H., Zhou, Y., Zheng, X., Liu, W. & Xu, Q. Single-layer 2D Ni-BDC MOF obtained in supercritical  $\text{CO}_2$ -assisted aqueous solution. *Chem. Eur. J.* **28**, e202201811 (2022).
51. Liang, H. et al. Novel photocatalyst based on through-space charge transfer induced intersystem crossing enables rapid and efficient

- polymerization under low-power excitation light. *Angew. Chem. Int. Ed.* **63**, e202402774 (2024).
52. Bo, Y. et al. Tuning the absorption, fluorescence, intramolecular charge transfer, and intersystem crossing in spiro[fluorene]acridinone. *Angew. Chem. Int. Ed.* **63**, e202313936 (2024).
  53. Liang, H. et al. Efficient intersystem crossing and long-lived charge-separated state induced by through-space intramolecular charge transfer in a parallel geometry carbazole-bodipy dyad. *Angew. Chem. Int. Ed.* **62**, e202312600 (2023).
  54. Lv, M. et al. Engineering the charge-transfer state to facilitate spin-orbit charge transfer intersystem crossing in spirobisanthracenediones. *Angew. Chem. Int. Ed.* **59**, 22179–22184 (2020).
  55. Ni, J. et al. Deep-blue electroluminescence from phosphine-stabilized Au<sub>3</sub> triangles and Au<sub>3</sub>Ag pyramids. *Angew. Chem. Int. Ed.* **61**, e202213826 (2022).
  56. Qi, Q. et al. Remarkable turn-on and color-tuned piezochromic luminescence: mechanically switching intramolecular charge transfer in molecular crystals. *Adv. Funct. Mater.* **25**, 4005–4010 (2015).
  57. Alfuth, J. et al. Cooperativity of halogen- and chalcogen-bonding interactions in the self-assembly of 4-iodoethynyl- and 4,7-bis(iodoethynyl)benzo-2,1,3-chalcogenadiazoles: crystal structures. Hirshfeld surface analyses, and crystal lattice energy calculations. *Cryst. Growth Des.* **22**, 1299–1311 (2022).
  58. Kresse, G. & Furthmüller, J. Efficiency of ab-initio total energy calculations for metals and semiconductors using a plane-wave basis set. *Comput. Mater. Sci.* **6**, 15–50 (1996).
  59. Hafner, J. Ab-initio simulations of materials using VASP: density-functional theory and beyond. *J. Comput. Chem.* **29**, 2044–2078 (2008).
  60. Perdew, J. P., Burke, K. & Ernzerhof, M. Generalized gradient approximation made simple. *Phys. Rev. Lett.* **77**, 3865–3868 (1996).
  61. Casida, M. E., Jamorski, C., Casida, K. C. & Salahub, D. R. Molecular excitation energies to high-lying bound states from time-dependent density-functional response theory: characterization and correction of the time-dependent local density approximation ionization threshold. *J. Chem. Phys.* **108**, 4439–4449 (1998).
  62. Stratmann, R. E., Scuseria, G. E. & Frisch, M. J. An efficient implementation of time-dependent density-functional theory for the calculation of excitation energies of large molecules. *J. Chem. Phys.* **109**, 8218–8224 (1998).
  63. Becke, A. D. Density-functional thermochemistry. III. The role of exact exchange. *J. Chem. Phys.* **98**, 5648–5652 (1993).
  64. Lee, C., Yang, W. & Parr, R. G. Development of the Colle-Salvetti correlation-energy formula into a functional of the electron density. *Phys. Rev. B* **37**, 785–789 (1988).
  65. Chai, J.-D. & Head-Gordon, M. Long-range corrected hybrid density functionals with damped atom-atom dispersion corrections. *Phys. Chem. Chem. Phys.* **10**, 6615–6620 (2008).
  66. Vreven, T. et al. Combining quantum mechanics methods with molecular mechanics methods in ONIOM. *J. Chem. Theory Comput.* **2**, 815–826 (2006).
  67. Dapprich, S., Komáromi, I., Byun, K. S., Morokuma, K. & Frisch, M. J. A new ONIOM implementation in Gaussian98. Part I. The calculation of energies, gradients, vibrational frequencies and electric field derivatives. *J. Mol. Struct. (Theochem)* **461**, 1–21 (1999).
  68. Wu, M. et al. Pressure-induced restricting intermolecular vibration of a herringbone dimer for significantly enhanced multicolor emission in rotor-free truxene crystals. *J. Phys. Chem. Lett.* **13**, 2493–2499 (2022).
  69. Breneman, C. M. & Wiberg, K. B. Determining atom-centered monopoles from molecular electrostatic potentials. The need for

high sampling density in formamide conformational analysis. *J. Comput. Chem.* **11**, 361–373 (1990).

## Acknowledgements

This work is supported by the National Key R&D Program of China (Grant No. 2023YFA1406200 to X.Y.) and the National Natural Science Foundation of China (Nos. 12274177 to X.Y., 22122307 and 22073099 to W.T., 22403093 to Y. Yin), The Kawai-Type Large-Volume Press experiments were performed at the B1 and B2 stations, Synergetic Extreme Condition User Facility (SECUF). This work was mainly performed at BL15U1 at the Shanghai Synchrotron Radiation Facility (SSRF). The authors thank the staff from SSRF at BL15U1, and User Experiment Assist System.

## Author contributions

X.Y. conceived the idea and designed the research. T.Z. prepared the sample and performed in-situ high-pressure experiments and analyzed data. Y. Yin and W.T. performed fs-TA measurements experiments and analyzed data. Y. Yang and W.W. assisted in performing experiments. T.Z., N.L., and F.B. carried out the theoretical calculation. X.Y., W.T., F.B., and B.Z. intensively discussed on the data and manuscript. T.Z. wrote the manuscript. All authors discussed and commented on the manuscript and contributed to the writing of the manuscript. T.Z. and Y. Yin contributed equally to this work.

## Competing interests

The authors declare no competing interests.

## Additional information

**Supplementary information** The online version contains supplementary material available at <https://doi.org/10.1038/s41467-025-59552-1>.

**Correspondence** and requests for materials should be addressed to Xinyi Yang, Wenming Tian, Fuquan Bai or Bo Zou.

**Peer review information** *Nature Communications* thanks Ze Chang, Zheng Wang, and Dongpeng Yan for their contribution to the peer review of this work. A peer review file is available.

**Reprints and permissions information** is available at <http://www.nature.com/reprints>

**Publisher's note** Springer Nature remains neutral with regard to jurisdictional claims in published maps and institutional affiliations.

**Open Access** This article is licensed under a Creative Commons Attribution-NonCommercial-NoDerivatives 4.0 International License, which permits any non-commercial use, sharing, distribution and reproduction in any medium or format, as long as you give appropriate credit to the original author(s) and the source, provide a link to the Creative Commons licence, and indicate if you modified the licensed material. You do not have permission under this licence to share adapted material derived from this article or parts of it. The images or other third party material in this article are included in the article's Creative Commons licence, unless indicated otherwise in a credit line to the material. If material is not included in the article's Creative Commons licence and your intended use is not permitted by statutory regulation or exceeds the permitted use, you will need to obtain permission directly from the copyright holder. To view a copy of this licence, visit <http://creativecommons.org/licenses/by-nc-nd/4.0/>.

© The Author(s) 2025